Microfabricated Quantum Dot Linked Immuno-Diagnostic Assay (QLIDA) Biosensor with Electrothermally Accelerated Biomolecular Binding

A Thesis

Submitted to the Faculty

of

Drexel University

by

Chengjie Yu

in partial fulfillment of the

requirements of the degree

of

Master of Science in Biomedical Engineering

December 2011

Dedications

To my parents, and dear Dr. Elisabeth Papazoglou

Acknowledgements

This thesis would not exist without the guidance, encouragement, and support from many individuals.

First and foremost, I would like to express my gratitude to Dr. Elisabeth Papazoglou, and Dr. Moses Noh, for their assistance and oversight of all my research endeavors during my graduate studies. They offered me the resources and freedom needed to complete the project. Moreover, Dr. Papazoglou was not only my academic advisor, but also my mentor. May she rest in peace.

I also would like to thank Dr. Wan Shih and Dr. Kambiz Pourrezaei for serving on my committee, and for their guidance and the valuable feedback that they have generously offered during the completion of this work.

I would like to express my gratitude to all administrative staff of the School of Biomedical Engineering at Drexel University for their support throughout my academic career.

I would like to thank Dr. Nadarajan Sundar Babu, Dr. Leonid Zubkov, Dr. Mike Neidrauer, Mr. Nikolay Voznyak, Mrs. Rosemary Bastian, Mr. David Hansberry, and Mr. Peter Clark.

Table of Contents

List of Tables

List of Figures

Abstract

Microfabricated Quantum Dot Linked Immuno-Diagnostic Assay (QLIDA) Biosensor with Electrothermally Accelerated Biomolecular Binding

Chengjie Yu

Optically transduced microfluidic immunoassays have proven to be a highly sensitive and rapid method to assess the concentrations of analytes in a biological fluid. Although microfluidic immunoassays facilitate higher throughput and automation than standard microtiter plates, the immunoreaction within such devices remains diffusion-limited unless the analyte concentration is high enough to compensate the diffusion limit. We aim to circumvent this issue and accelerate the immunoreaction by developing a microfluidic immunosensor with an integrated set of electrodes to facilitate perpendicular electrothermal flow due to joule heating. In this work, 1) particle behaviors under AC electrohydrodynamic conditions, especially eletrothermal effect (ETE), has been studied, and 2) microfluidic biosensor devices with electrothermal mixing elements have been designed and developed. The Maxwell stress tensor method was used to understand dielectrophoretic particle-particle interactions. We applied the results of this to the interpretation of particle behaviors under dielectrophoresis (DEP) and electrothermal effect (ETE) conditions. Distinct particle behaviors ETE are presented and analyzed. Moreover, diverse particle-particle interactions are observed in experiments. These include particle clustering wherein particles keep a certain distance from each other, chain formation, and disc formation. These behaviors are explained by numerical simulation data (COMSOL Multiphysics v3.5a). After studying fluid motion under AC electrohydrodynamic condition, microelectrodes, the key elements to generate ETE, was

integrated into microfluidic immune-biosensor using microfabrication technique. Microfluidic channels serve as solid phase in immunoassay, that were fabricated on inexpensive poly methylmethacrylate (PMMA) sheets by a solvent-based polymer imprinting and binding method. The microfluidic biosensors take advantage of quantum dots (QDs) as fluorescence probes. A low cost UV-LED was used as an excitation source, and data were collected by a CCD camera. Electrothermal effect increases the possibility of antibody-antigen binding by actively transporting analyte to the sensing part. With the enhancement of ETE, the time spent on the core part of immunoassay has been significantly reduced from 3.5 hours to 30 minutes.

CHAPTER 1: INTRODUCTION

1.1 Motivation

Enzyme-linked immunosorbent assay (ELISA), a biochemical technique used as a diagnostic tool, has been widely used and reported since 1970s[1], for it provides ideal systems for dealing with a wide range of studies in many biological areas, such as HIV test[2-4], food allergens detection[5, 6], hepatitis detection[7, 8]. However, conventional ELISA usually is conducted in a 96-well plate, which requires more than 50 μl of certain expensive reagents, especially antibodies. In addition to the cost inefficiency of ELISA, it is also time consuming to complete an assay, often taking hours to a day because of the transport limited nature of the system. This can be a critical barrier to the creation of many types of biosensors which would require timely detection results.

Microfluidics emerged in the beginning of the 1980s[9]. Since then, it has become one of the fastest developing disciplines of microtechnology with the breakthrough of microfabrication. Microfabrication offers miniaturization of devices, enabling the manipulation of small liquid volumes, resulting in portable and inexpensive devices. The advantages that microfluidic immunosensor platforms have over standard microtiter plate based assays arise from their higher surface area to volume ratio while allowing the use of smaller working volumes with decreased characteristic diffusion lengths for biomolecules.

A low cost and fast detection immunosensor with an active mixing element has been proposed here. The proposed device takes the advantages of microfluidic devices and the

optical properties of quantum dots. It is hoped that the results of this research will help to reduce the reaction time, and increase the sensitivity in a cost-effective way.

1.2 Overall Objective

The objective of this project is to develop a microfabricated poly(methyl methacrylate) (PMMA) quantum-dot-linked-immuno-diagnostic-assay (QLIDA) biosensor with embedded mixing element. Our team has developed a microcapillary QLIDA assay in PMMA capillaries [10], with sensitivity comparable to ELISA yet using sample volumes 1/100th of those used in traditional ELISA. The advantages realized by the innovative QLIDA method such as the simplicity of testing, minute volumes of sample and reagents needed, and the inexpensive detection can be extended further by integrating the methodology in a microfabricated platform. The capability to generate micro and nanostructures on the PMMA microchannel is well established; one is not limited to the commercially available PMMA capillaries but can optimize surface morphology to increase sensing area. Moreover, our preliminary studies strongly support the notion that the inclusion of mixing capability in situ will greatly enhance sensor kinetics that are based on thermal diffusion of molecules in the microchannel environment. It is believed that the proposed addition of active mixing element will enable further reduction of assay time and can increase selectivity.

Thus, the specific aims of this particular project are as follows:

(a) Design, fabrication, and testing of PMMA microchannel for QLIDA

(b) Incorporation of electrokinetic mixing onto the PMMA microchannel

CHAPTER 2: BACKGROUD

2.1 Introduction to Biosensors

According to the International Union of Pure and Applied Chemistry (IUPAC), a biosensor can be defined as a device that uses specific biochemical reactions mediated by isolated enzymes, immunosystems, tissues, organelles or whole cells to detect chemical compounds usually by electrical, thermal or optical signals[11]. According to IUPAC, a biosensor consists of three basic components: the biorecognition molecule that recognizes and binds the target of interest with high selectivity, the transducer that converts the binding reaction into a measurable signal, and the output system which amplifies and displays the signal in a useful form. Figure 1 shows the basic components of a biosensor.

Due to the advantages that biosensors have over traditional analytical methods, the applications of biosensors has boomed since 1956[12]. These advantages include better performance, portability, high selectivity, and so on. Biosensors are widely used in many areas, including the medical field[12-14], the pharmaceutical field[15-18], the monitoring and protection of the environment[19-21], the food industry[21-24], and the military.

Among the various transduction mechanisms, three main categories of methods have received the most attention[11]. The categories are optical, electrochemical and electromechanical. Optical techniques are the most widely investigated method due to their fast detection, sensitivity, and the advantage of non-destructive measurement.

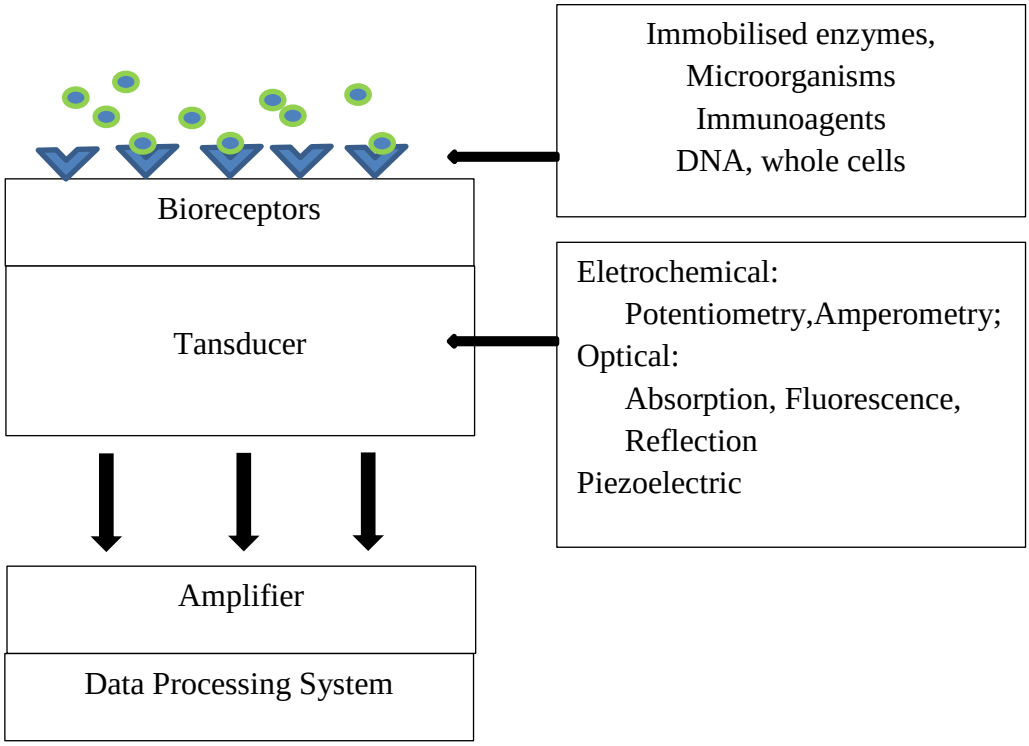

Figure 1 Schematic representation of the basic components of a biosensor. It consists of bioreceptors with biorecongnition molecules attached, a transducer, and an output system.

2.2 ELISA

Enzyme-linked immmunosorbent assay (ELISA) consists of the immobilization of an analyte to a surface followed by subsequent immunological reactions such as the antibody-antigen reaction [1]. The detecting antibody is linked to an enzyme, usually horse radish peroxidase (HRP). The enzyme reacts with substrate in the final substance solution that is added in the final step, generating the quantifiable signals, most commonly a color change in the substrate, which can be detected by colorimeter.

ELISAs come in three main types – the Direct ELISA, the Indirect ELISA, and the Sandwich ELISA[1]. Direct ELISA is the simplest form of ELISA, in which antigen is passively absorbed by the substrate (the solid phase), followed by a washing step to remove unbound antigen. Enzyme-linked antibodies are then added, and the enzyme's substrate is added for developing color after an incubation and a washing step. Figure 2 shows the schematic of the Direct ELISA procedures. Indirect ELISA is similar to the direct system in that the antigen is first directly attached to the solid phase and is the target for detecting antibodies. Unlike the direct system, the added antibodies do not link to enzyme molecules, but are themselves targeted by another antibody (the secondary antibody) that is labeled with enzyme.

In the Sandwich ELISA, the main difference from Direct or Indirect ELISA is that a layer of antibody is first introduced into the systems for capturing antigen. The purpose of this strategy is to reduce nonspecific binding of undesired protein, because without the

first layer of capture antibody, any protein in the sample may competitively adsorb to the substrate surface, lowering the quantity of antigen immobilization.

Despite its age, ELISA has remained the technique of choice. Furthermore, ELISA has experienced a wide array of enhancements since its initial development. Although it shows excellent sensitivity, its two major drawbacks are the lengthy enrichment procedure and the consumption of expensive reagents, such as antibodies.

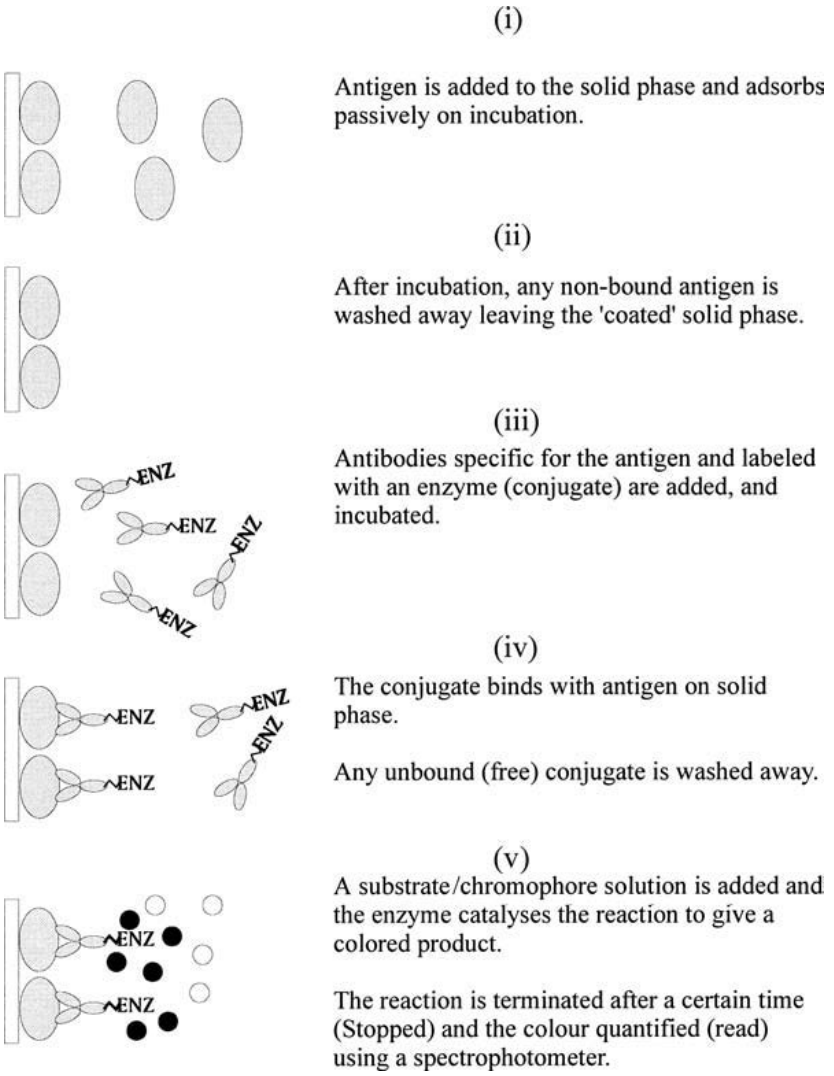

Figure 2 Direct ELISA. First antigen is attached to the solid phase by passive adsorption, followed by a washing step. Then, enzyme-labeled antibodies are added. After incubation and washing, an enzyme substrate is added and color is allowed to develop for measurement.[1] (Adapted from The ELISA guidebook)

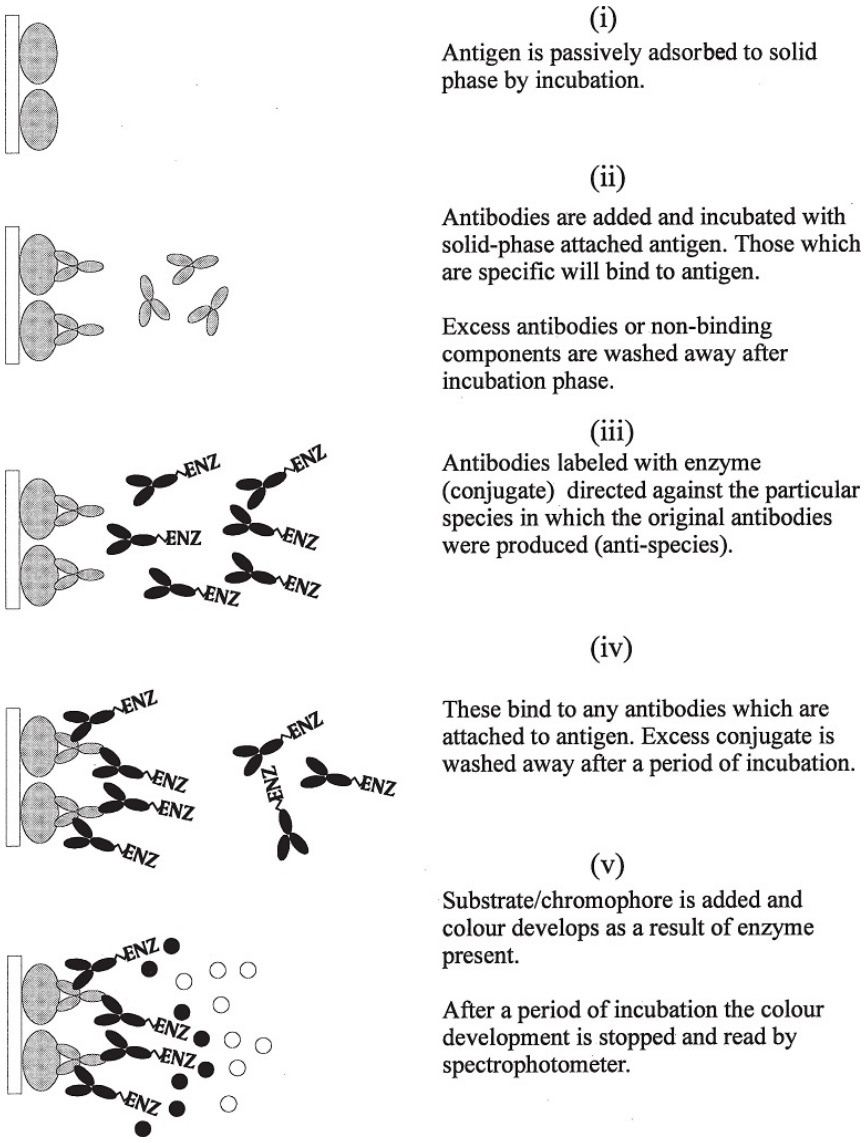

Figure 3 Indirect ELISA. First antigen is attached to the solid phase by passive adsorption. Primary antibodies capture the antigen attached to the solid phase. Secondary antibodies are labeled with an enzyme that targets the primary antibodies. This is widely used in diagnosis.[1] (Adapted from The ELISA guidebook)

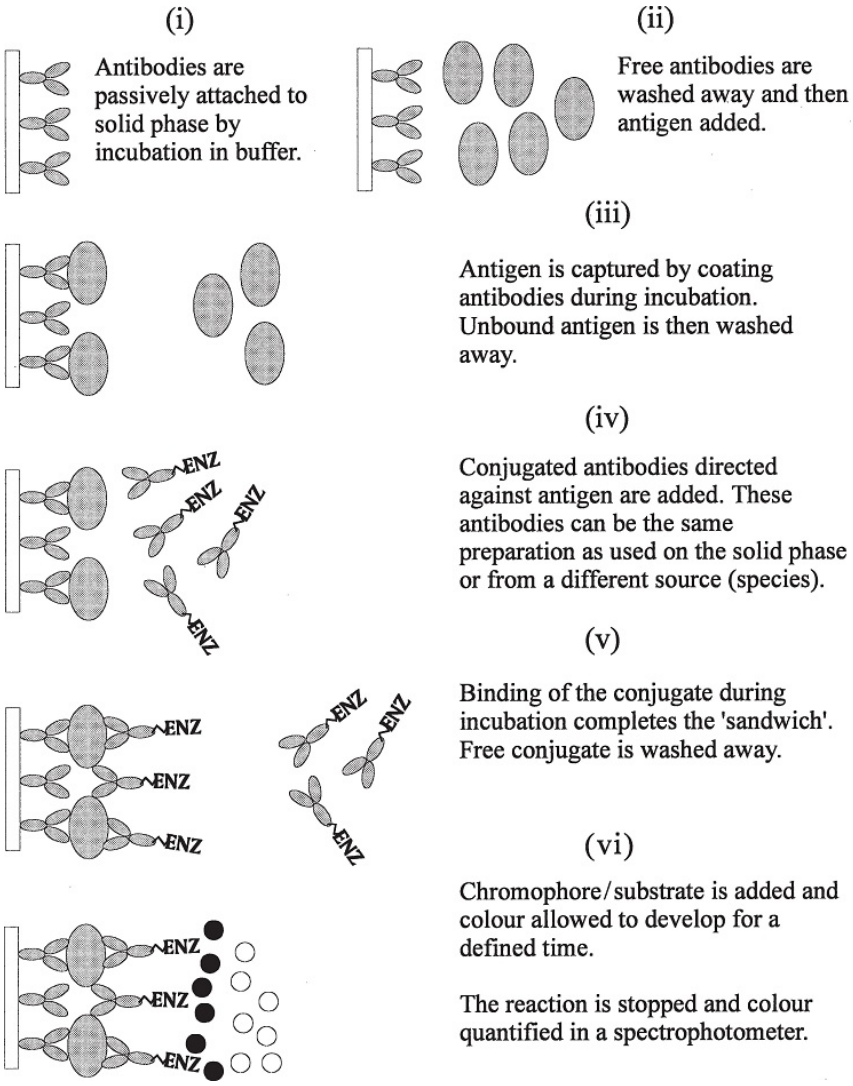

Figure 4 Sandwich ELISA. A layer of antibodies, called capture antibodies, is first passively adsorbed on the surface of solid phase. Then, antigen is added and captured by the first layer or antibodies. The antigen is then detected by another antibody, the detecting antibody, which is labeled with enzyme. [1] (Adapted from The ELISA guidebook)

A heterogeneous fluorescent immunoassay can be completed in much the same way as an ELISA. In this case, an enzyme-linked secondary antibody is replaced with a fluorescently labeled secondary antibody. The conventional fluorescent dyes, such as fluorescein isothiocyanate (FITC), have many disadvantages, such as a narrow excitation range, low fluorescence intensity, and a short lifetime.

Quantum dots (QDs) are a novel and outstanding nanomaterial with various promising applications and advantages over other materials due to their distinguished photoluminescence and electroluminescence properties. After being excited by photons or an electric field, QDs release energy by emitting photons as they return to their rest state. Moreover, the emission energy is controllable by selecting the composition and the particle size of the quantum dots (Figure 5(a)) due to the quantum confinement effect[25].

Unlike traditional organic dyes, QDs can be excited by broad spectra, but the emission spectra are narrow and strong (Figure 5(b)). This uniquity allows the simultaneous observation of multiple probes with different fluorescent colors using a single light source. With an extraordinary photostability that is much greater than that of organic dyes, QDs make the long-term real-time monitoring and tracking of molecules and cells more feasible.

(a)

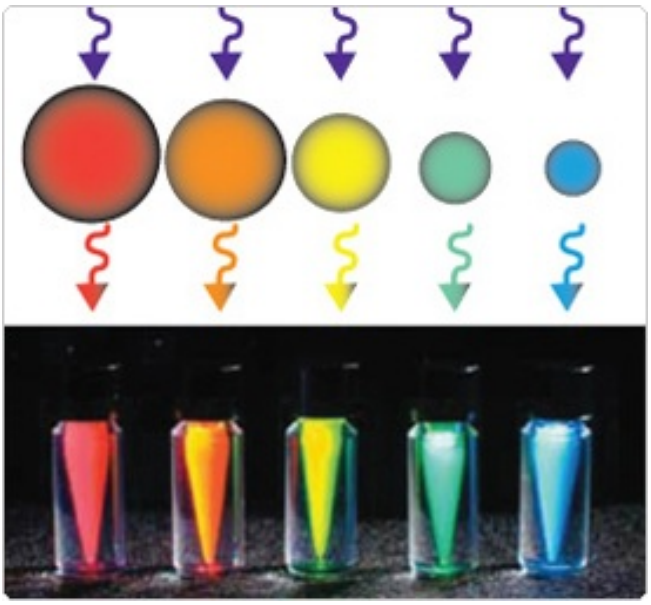

(b)

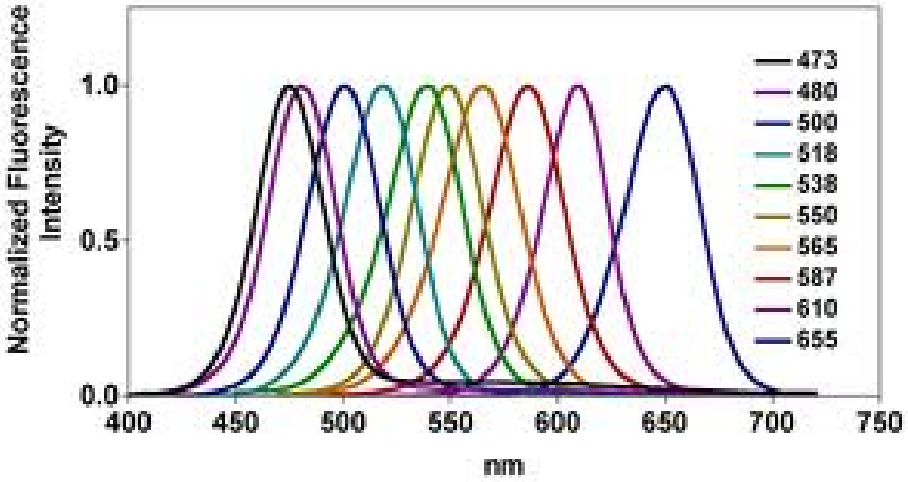

Figure 5 (a) with the same excitation source, five different QDs emit different fluorescences; the size of the QDs determines the color. (Adapted from Invitrogen Website). (b) QDs can be excited by broad spectra, but the emission spectra are narrow and strong. (Adapted from Altman Laboratory, Emory Vaccine Center)

Microfluidics can be defined as the study of lows that are simple or complex, mono- or multiphasic, which are circulating in artificial microsystems[9]. The systems are fabricated using microfabrication technologies, including photolithography, etching, deposition, microwetting, and mciroimpression. Microfluidics enables the control, manipulation, and understanding of the behavior of tiny volumes of liquid, ranging from a few microliters to a few femtoliters. Microfluidic devices are usually fabricated on silicon wafers, glass, metals such as stainless steel, and polymers such as polydimethylsiloxane (PDMS). Due to the large surface area-to-volume ratio, experimental performance can be enhanced in microfluidic devices. The advantages of the miniature features of microfluidic devices also include portability, cost effectiveness in manufacturing and sample handling, and the ability to more closely mimic biological systems on the cellular level.

Fluids behavior on the microscale is far different from macrosystems. In microsystems, surface tension, dissipation of energy, resistance, and viscosity dominate[9]. One of the major features is the extremely low Reynold's number, which is usually less than 100. The Reynold's number (Re) is a common dimensionless parameter in fluid mechanics and is the ratio of inertial forces to viscous force. The Reynold's number shows the relative importance of inertial forces versus viscous forces under different fow conditions. The Reynold's number can be expressed as:

$$Re = \frac{\rho v_s L}{\mu} = \frac{v_s L}{\nu} = \frac{Inertial\ Forces}{Viscous\ Forces} \quad (1)$$

where ν_s is the mean fluid viscosity, L is the characteristic length, μ is the absolute dynamic fluid viscosity, ν is the kinematic fluid viscosity, and ρ is the fluid density. Laminar flow is identified by a Reynold's number less than 2300. It is common that the Reynold's number is less than 100 in a microfluidic system, which means all the mixing and interaction in the microscale systems is solely based on diffusion. Thus, if there is no effective mixing mechanism integrated into microfluidic systems, fast reaction or fast detection is still hard to achieve.

2.5 AC electrokinetics

AC electrokinetics is the study of fluid movement and particle behaviors in suspension using AC electric fields[26]. The study of the motions of particles and fluids in DC fields have been studied for over 100 years, while the study of the behaviors of particles and movement of fluids in AC field only started three decades ago, when Herbert Pohl discovered the dielectrophoresis (DEP) in 1970s[27]. By taking the advantages of the development of microfabrication, AC electrokinetic particle and fluid study is readily achieved in a micro device via non-uniform electric fields. High electric fields ($10^4 \sim 10^6$ V/m) can be easily generated from a small applied AC potentials, since the electrode gap is micro- or nanoscale, avoiding using high electric potential. By placing the microelectrodes locally inside a microchannel, experimental flexibility is highly increased because of the integration of different components onto a single chip. Moreover, by applying high frequency electric fields, electrolysis can be reduced or eliminated in an AC electric field. The potential of AC electrokinetic techniques have been undoubtedly proven, and AC electrokinetic techniques are widely used in microfluidic devices and

lab-on-a-chip systems for a variety of research fields, such as manipulation of polymer micro-/nanospheres[28], cells[29], bacteria[30], and DNA[31].

AC electrokinetic phenomena include the AC Electrothermal Effect (ETE), dielectrophoresis (DEP), and AC eletroosmosis (ACEO). These phenomena result from numerous physical processes, such as interfacial polarization, the formation of an electric double layer, heat dissipation in media, etc. DEP moves particles towards higher electric field strength (positive DEP) or lower electric field strength (negative DEP), which occurs when a particle is polarized in a non-uniform AC electric field. ACEO and ETE, unlike DEP, are hydrodynamic phenomena. When an AC potential is applied, an induced electrical double layer will form at the electrode surface, where induced charges will experience a force due to the action of the tangential field, causing fluid motion, which is known as AC electroosmosis. ETE is caused by temperature gradients induced by joule heating inside the media when a high electric field applied. AC electrokinetics is subject to a variety of factors, such as polarizability of particles, electric field strength, frequency, medium conductivity and permittivity, etc. For example, high media conductivity suppresses the ACEO and prohibits positive DEP. Figure 6 illustrates three AC electrokinetic phenomena[32].

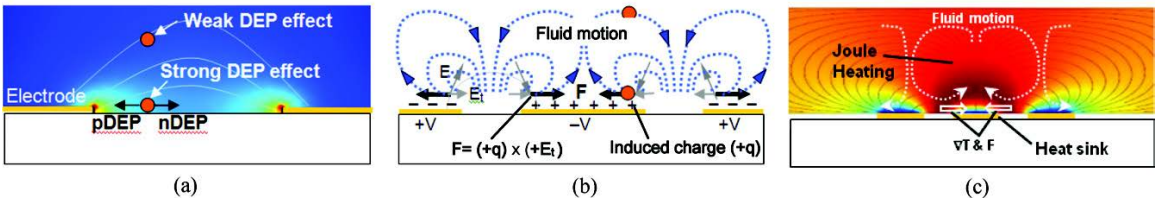

Figure 6 AC electrokinetic phenomena. (a) Dielectrophoresis (DEP), (b) AC electroosmosis (ACEO), and (c) Eletrothermal effect (ETE).

2.5.1 AC electrothermal effect

When an electric field is passed through a liquid, the passage of current results in Joule heating and generates a spatial temperature gradient according to the following heat transfer formula:

$$k\nabla^2 T + \sigma E^2 = \rho c_p V \cdot \nabla T \qquad (2)$$

where k is the thermal conductivity , T is the temperature in Kelvin, σ is the electrical conductivity and E is the magnitude of the electric field. The electrical conductivity and permittivity vary according to the temperature gradient. The relationship between temperature and electrical parameter variations can be defined as follow [33]:

$$\left(\frac{1}{\varepsilon}\right)\left(\frac{\Delta\varepsilon}{\Delta T}\right) = -0.004\ K^{-1} \qquad (3)$$

$$\left(\frac{1}{\sigma}\right)\left(\frac{\Delta\sigma}{\Delta T}\right) = 0.02\ K^{-1} \qquad (4)$$

The hydrodynamic force resulting from the electrical property gradient can be expressed as[34]:

$$f_{ETE} = -0.5\left[\left(\frac{\nabla\sigma}{\sigma} - \frac{\nabla\varepsilon}{\varepsilon}\right)E \cdot \frac{\varepsilon E}{1+(\omega\tau)^2} + 0.5|E|^2 \cdot \nabla\varepsilon\right] \qquad (5)$$

where τ is the charge relaxation time (ε/σ). This hydrodynamic force of fluid motion is called eletrothermal force. The electrothermal effect is usually used for higher conductivity media because with lower the fluid impedance more energy can pass through the liquid, causing stronger Joule heating effects. Generally speaking, when the frequency of the applied potential and the medium conductivity is high (f > 80 kHz, σ > 100 μS/cm), ETE dominates the fluid motion, while ACEO diminishes. Fluid velocity because of ETE increases much more dramatically with an increase in voltage due to a fourth power relationship between velocity and applied voltage. Therefore, doubling the velocity results in a 16 times increase in fluid velocity.

2.5.2 Other AC electrokinetic phenomena: DEP and ACEO

2.5.2.1 Dielectrophoresis

When any particle, including biological particles, is suspended in an electrolyte, an electrical double layer will form around the suspended particle[34]. An electric field will generate force on a particle with a dipole (induced or permanent). In a uniform electric field, the force on each of the two poles of the dipole is equal and opposite, so that there is no movement. However, if the field is non-uniform then the two forces are not equal, and the particle moves. The direction of movement depends on the difference in the polarizability of the particles and the surrounding medium. In other words, if the fluid is less polarizable than the particle, the particle will experience positive DEP, moving towards the region of high field strength. In contrast, particles will experience negative DEP if the particle is less polarizable than the fluid. Polarizability depends on many factors, such as the three dimensional particle geometry (interior and exterior), the

properties of its constituent material, the frequency of an applied electric field, and the conductivity of the media[35].

2.5.2.2 AC electroosmosis

An electric double layer is formed when an AC electric field is applied to planar electrodes, where mobile counter ions in an electrolyte are attracted to the electrode surface[34-36]. In the case of planar electrode geometry, the counter ions are pulled along the tangential component of the applied electric field, from the edge to the center of the electrode. The direction of movement does not change with the polarity change of the AC electric field, due to the counter ions being switched as well. The motion of the ions drags the bulk fluid along the surface.

In low conductivity media, such as DI water, ACEO can be observed. On the contrary, in high conductivity media, such as phosphate buffer solution, an immovable electric double layer forms, resulting in no ion-movement. ACEO is highly dependent on frequency. At low and high frequency, the ACEO is suppressed, whereas, the fluid velocity reaches a maximum at mid-range frequencies.

Chapter 3: Flow Characterization under AC Electrohydrodynamic Condition

3.1 Device Fabrication and Materials

The experimental devices are composed of a microchannel and a gold microelectrode substrate. The gold planar interdigitated electrodes were fabricated on glass substrates or on silicon wafers with a 200 nm thick oxide layer. A 20 nm thick chrome layer was first deposited on the substrate, followed by the deposition of a 200 nm thick gold layer using thermal evaporation. Then a photoresist (Shepley 1827) was spin-coated (3000 rpm, 1000 r/s, 30 s) on the gold surface, followed by a standard photolithography (120 mJ/cm^2 dose) to create a patterned mask for the subsequent etching process. Unprotected gold and chrome layers were etched away by gold etchant trifluoroacetic acid (TFA) and chromium mask etchant, subsequently. The schematic process of device fabrication is shown in Figure 7(a). Figure 7(b) shows the interdigitated electrode of a width of 93 μm and a gap of 33 μm.

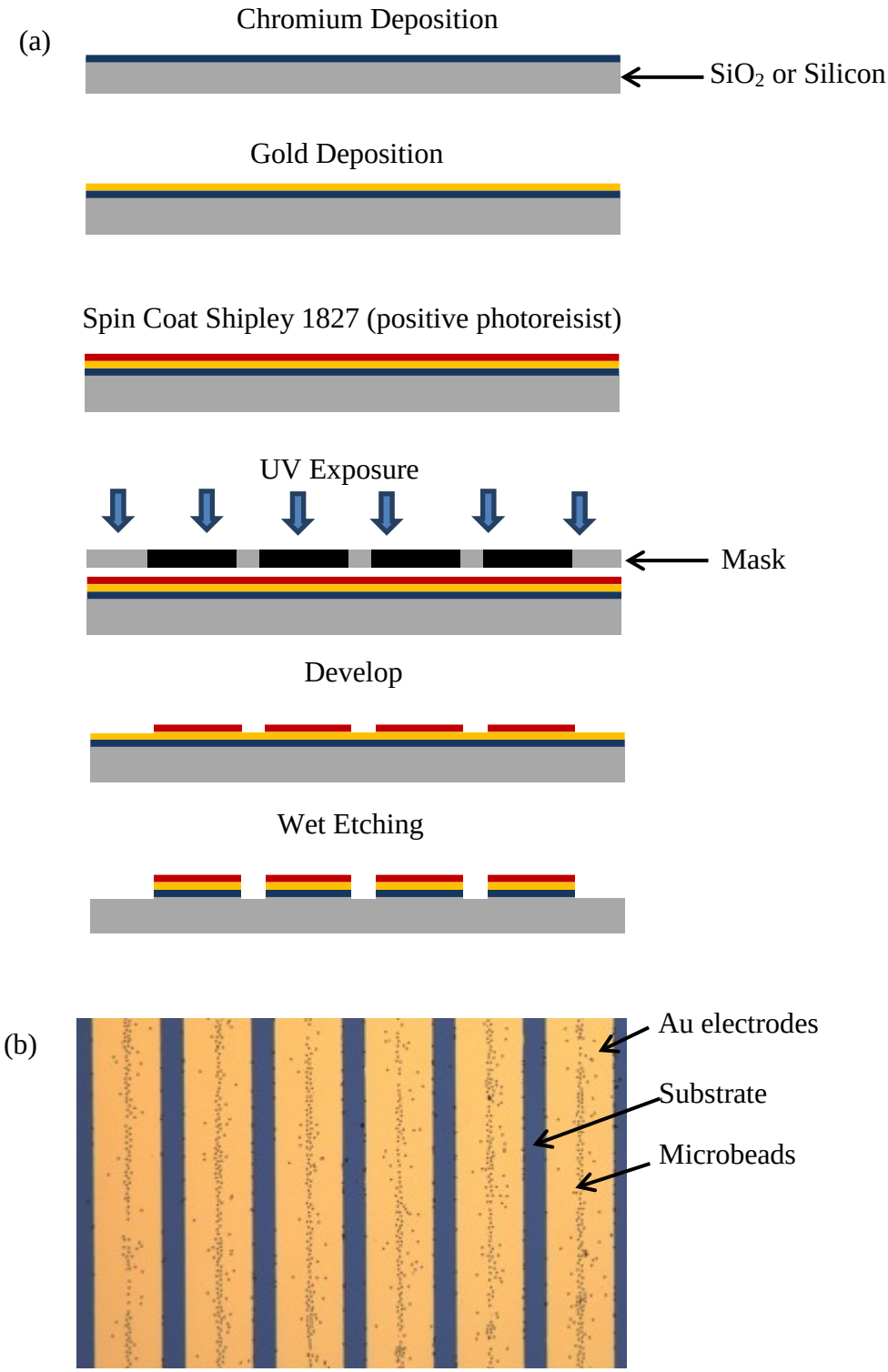

Figure 7 (a) Schematic of microelectrodes fabrication process. (b) 93 μm microelectrodes with 33 μm gap

Microchannels were made of polydimethylsiloxane (PDMS). The replica molding technique was used to make PDMS microchannels. First, SU-8 (SU-8 2035) master molds were made on a silicon wafer, resulting in 100 μm high molds. 3 inch Si wafers (University Wafer Inc.) were cleaned with piranha solution (98% sulfuric acid: Hydrogen peroxides = 3:1) for 10 min, followed by 2% HF cleaning for 3 min. After rinsing with DI water, the Si wafers were dehydrated at 150°C for 5 min. Hexamethyldisiloxane (HMDS) (MicroChem Corp.) was coated on the Si wafers for better adhesion of SU-8, and then they were dehydrated for another 5 min at 150 °C. Patterned SU-8 photoresist features were formed on the Si substrates using the following method. Negative photoresist, SU-8 2035 (MicroChem Corp.), was spun on a glass at 1000 rpm for 30 seconds, which yielded a thickness of 100μm, followed by soft baking at 65°C and 95°C for 10 and 30 minutes, respectively. After exposing the photoresist to UV light (19.8 mW/cm^2) through a patterning mask for 30 seconds, the wafer was baked at 65°C and 95°C for 15 minutes each. Then the SU-8 pattern was developed in SU-8 developer (MicroChem Corp.) for 20 minutes, and rinsed with isopropanol. Schematic of SU-8 master molds and PDMS microchannel fabrication is shown in Figure 8. Sylgard 184 base resin and curing agent (Dow Corning) were mixed at 10:1 ratio, followed by degassing in a vacuum dessicator for 30 minutes and baking at 80 °C for 2 hours. Then, PDMS channels (2 mm × 12 mm × 100 μm) were cut into individual devices and 0.3 mm holes were made as an inlet and outlet. In order to avoid leakage, gentle compression was applied after the PDMS microchannel was placed on top of the microelectrodes. Electrodes, via conductive adhesive, were attached to copper wires, which were connected to a function generator. In order to observe fluid motion, 2 μm polystyrene

microbeads (Polysciences, Inc) were added into 0.1 M phosphate buffered saline (PBS) to create a colloidal mixture. PBS is widely used in biological assays. The electric conductivity of 0.1 M PBS is 1.77 S/m.

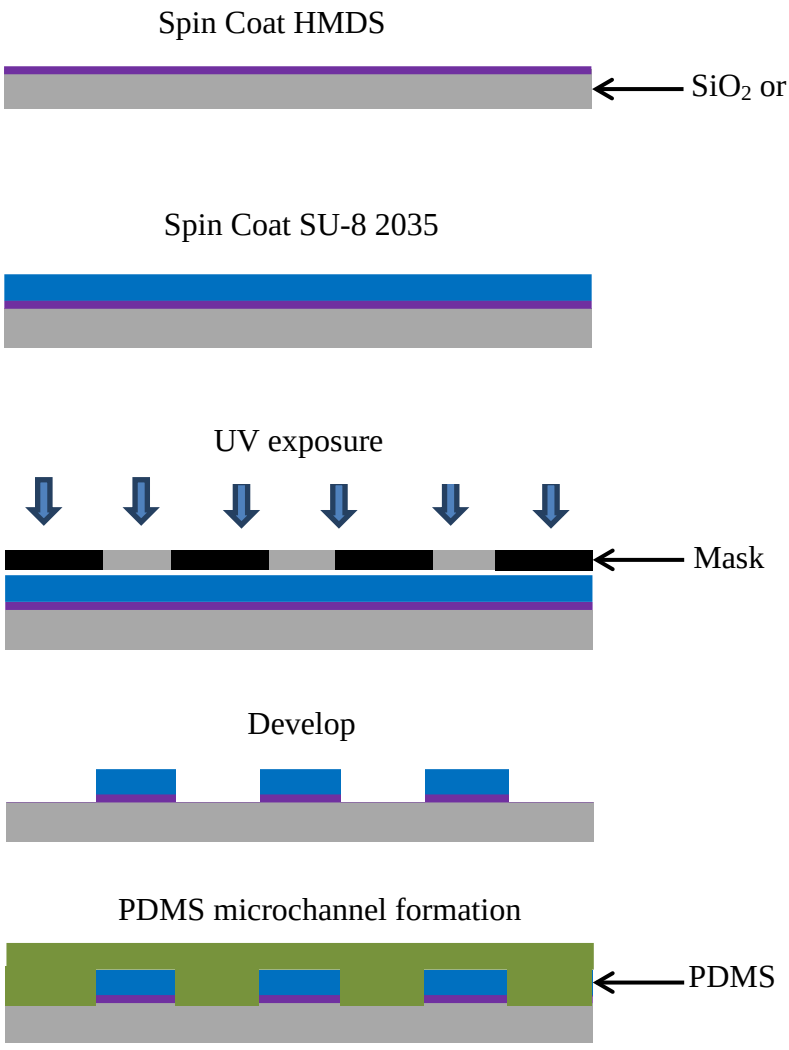

Figure 8 Schematic of PDMS microchannel fabrication process

3.2 Experimental Procedure

The experimental setup (Figure 9a) consisted of a microscope (Leica DM4000 B) equipped with two CCD (charge couple device) cameras (Leica DFC 420C; Moticam 2300), a function generator (Agilent 33250A 80MHz) and a voltage amplifier (Brüel&Kjær Type 2713), which was connected to an assembled device placed on the Peltier cooler (CP-031, TE technology) (Not shown). For these experiments, the voltage was increased incrementally from 3 to 10 V_{rms} in steps of 1 V_{rms}. Although different frequencies were tested in the experiment, a frequency of 200 kHz was the default setting for most of the tests. A Peltier cooler was used to maximize the temperature gradient and thus, enhance the ETE.

(a)

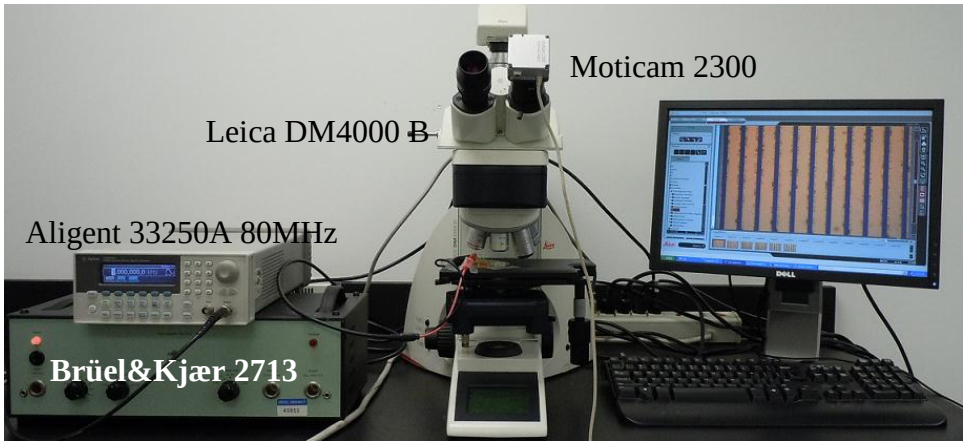

(b)

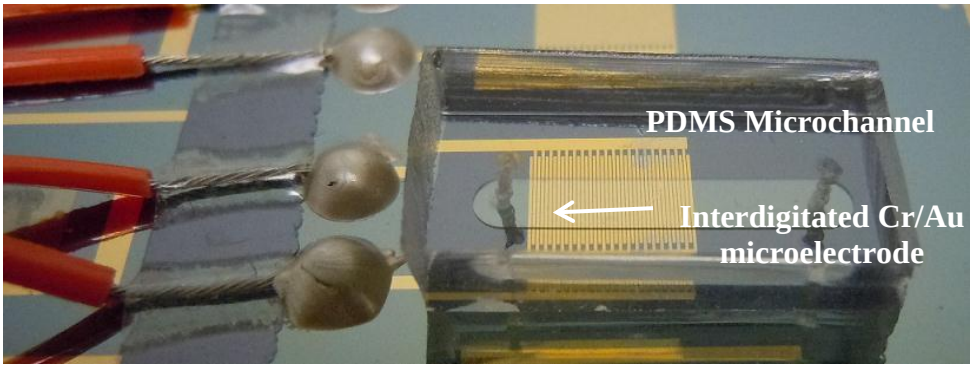

Figure 9 Pictures of (a) experimental set-up and (b) a device used in the experiments

COMSOL Multiphysics software version 3.5a was used for the simulation of ETE. The software is based on the finite element method. The element shapes were triangular for 2-D geometries and tetrahedral for 3-D geometries considered. The element type we used was the quadratic Lagrange element, and the maximum element length was set to 0.2 μm. With the help of complex number analysis, all current simulations fall into stationary problems.

The governing equation for the electric potential of a dielectric system is expressed by

$$\nabla(\varepsilon \nabla V) = 0 \qquad (6)$$

where ε is the complex permittivity and V is the electric potential. This equation is based on the assumption of no-net electric charge (negligible ion effect), harmonic oscillation (linear model) and negligible convection effects.

The electrothermal effect is simulated by the sequence of solving the electric (Eq. 6), the Navier-Stokes and the convection-conduction equations (Eq. 2). The Navier-Stokes equation that includes electrothermal force (Eq. 5) is Eq. 7.

$$\rho \frac{DV}{Dt} = -\nabla p + \eta \nabla^2 V + f_{ETE} \qquad (7)$$

The modeling conditions were taken to be similar to the experimental conditions. Long and repeating interdigitated electrodes are represented by the boundary conditions described in the figure. Physical parameters used for computation were $\varepsilon_{m,r}$ = 80, $\varepsilon_{p,r}$ = 2.5, $\sigma_{p,bulk}$ = 1×10^{-16} S/m and K_s = 1×10^{-9} S. V_{rms} = 3 ~ 7 V, $c_{p,m}$ = 4.184 kJ/(kg K), k_m =

0.598 W/(m K), σ_m = 1.77 S/m, $k_{silicon}$ = 149 W/(m K), $\rho_{silicon}$ = 2330 kg/m^3, and $c_{p,silicon}$ = 0.70675 kJ/(kg K).

Table 1 Summary of simulation parameters

Symbols		Values
V_{rms}	Applied voltage	3 ~ 7 V
$c_{p,m}$	Medium heat capacity	4.184 kJ/(kg K)
k_m	Medium thermal conductivity	0.598 W/(m K)
σ_m	Medium electric conductivity	1.77 S/m
$k_{silicon}$	Silicon thermal conductivity	149 W/(m K)
$\rho_{silicon}$	Silicon density	2330 kg/m^3
$c_{p,silicon}$	Silicon heat capacity	0.70675 kJ/(kg K)

3.4 RESULTS AND DISCUSSION

Figure 10 shows particle behaviors in an AC field of 4 V_{rms} and 200 kHz. Particle movement is dominated by ETE in this condition, while ACEO does not exist at such a high frequency or in media with such a high conductivity. The applied potential was gradually elevated, and the particles began to move above 3 V_{rms}, indicating that ETE took effect, with the existence of a Peltier cooler. The Peltier cooler was used to enhance the temperature gradient by creating heat sink at the bottom of substrate. The role of the Pertier cool in this experiment is significant in terms of the voltage threshold for triggering ETE and particle velocity. Immediately after applying an electric field, most of the particles followed a swirling motion above the electrodes edge (Figure 10). The flow pattern was similar to that of ACEO flow. Then, the particles formed short chains about 15 μm above the electrode edges in about three seconds after the potential was applied. The particles chains were perpendicular to the electrode when viewed from the top and kept the same distance from each other (about 3~7 μm). These phenomena can be explained by the combination of DEP and ETE forces. At a 200 kHz frequency, particles experienced negative DEP and were repelled from the electrode edges. As they entered the swirling zone of ETE, they experienced circular movement in a plane perpendicular to the electrodes. Particles rotated locally within a certain distance from the electrode edges. In the meantime, particles moved close to each other in the x direction and began to form chains at about 15 μm above the electrodes.

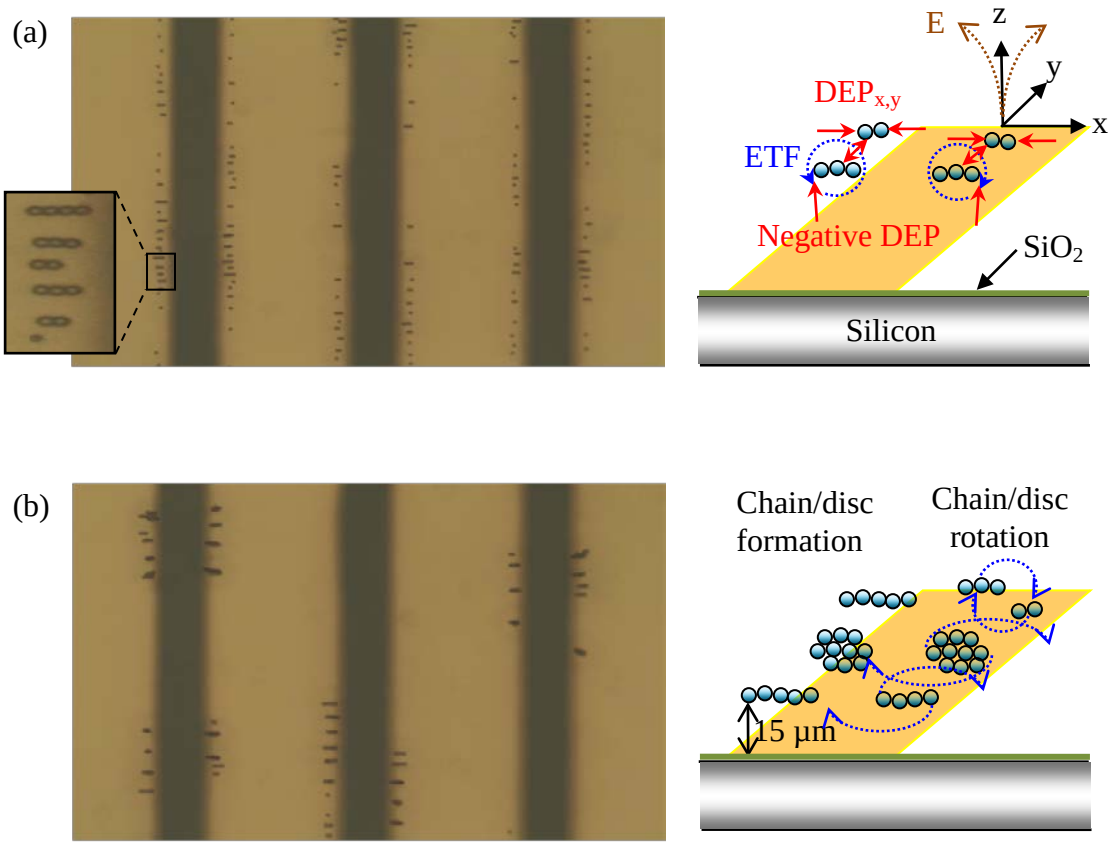

Figure 10 Behaviors of polystyrene microbeads under ETF condition (4 V_{rms} and 200 kHz), (a) 3 seconds after an electric field was applied (b) 3 minutes after an electric field was applied.

In order to better understand these phenomena, ETE was solved in a 2-D domain. Figure 11 shows the temperature profile contour plot, electric field streamlines and electrothermal flow arrows. Swirling zones were clearly observed and had good agreement with the experimental observation. The center of swirling motion was approximately 27 μm above the electrode (x = 36 μm and z = 27 μm). The location of particle chains in our experiment was approximately 15 μm above the electrode (z = 15 μm), right below the swirling zones. The reason why the particles were located below the swirling center may be due to the effect of gravity. In other words, the particle resting location of z = 15 μm seems to be the location where DEP, ETE, and gravity effects were balanced.

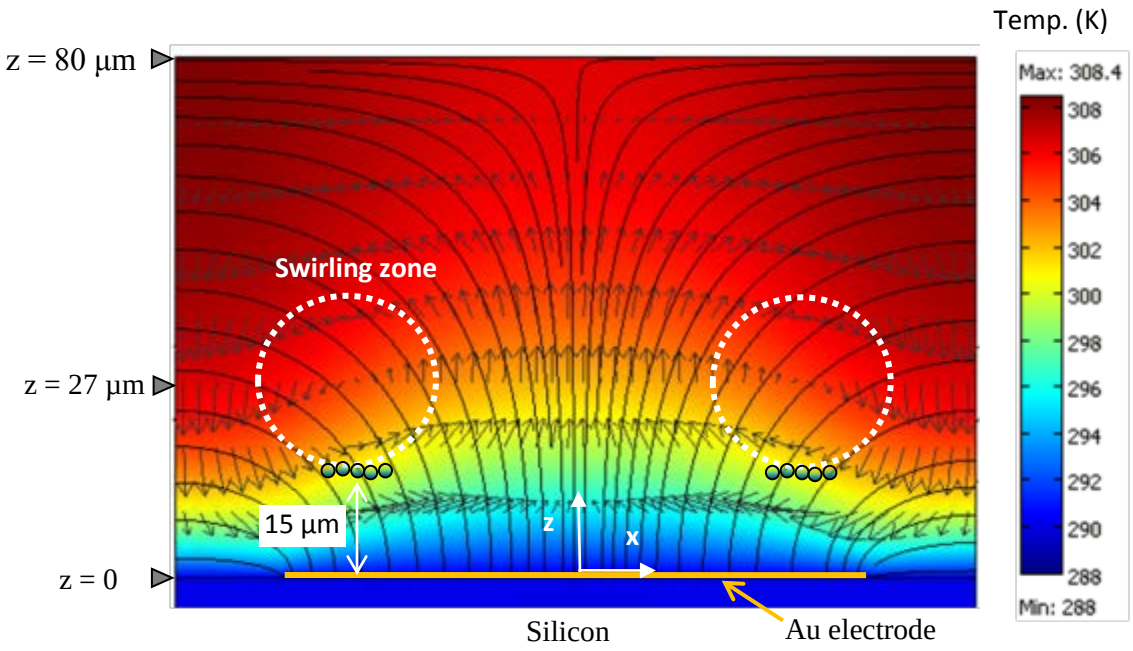

Figure 11 Electrothermal flow 2-D simulation result. The contour colors, the streamlines and the arrows represent temperature profile, electric field lines and electrothermal flow velocity, respectively. (σ_m = 1.77 S/m, f = 200 kHz, V_{rms} = 7 V)

The particle-particle dielectrophoretic interaction was investigated by placing a subject particle at the swirling center and another particle within a certain distance from the first particle. When the two particles were placed in the electric field direction 45^{o} from the normal direction of the electrode plane, attraction force was experienced by the particles (Figure 12a). As the particle distance decreased, the attractive DEP force increased significantly. This result supports the formation of particle chains and their alignment normal to the electrodes. When two particles were positioned in the y direction (perpendicular to the electric field), a repulsive DEP force was generated between them. Figure 12b shows how the repulsive DEP force varies with the distance between the two particles in y direction. As two particles get closer, the repulsive force increases. This result is consistent with the experimental observations that particle chains kept a distance from each other.

The particle chains became longer with time as they recruited more particles from the surrounding. Moreover, the particle chains formed near the swirling zones continued to rotate. Short chains rotated like a spinning rod while longer chains split into two short chains and switched their locations as shown in the schematic in Figure 10b. As time went on, the chains merged together into larger groups and particle “discs” were formed. It is not clearly understood why the particle chains merged with others and formed discs, but it seems that the attractive DEP particle-particle interaction in the electric field direction overcame the repulsive DEP particle-particle interaction in the direction perpendicular to the electric field as the chains became longer.

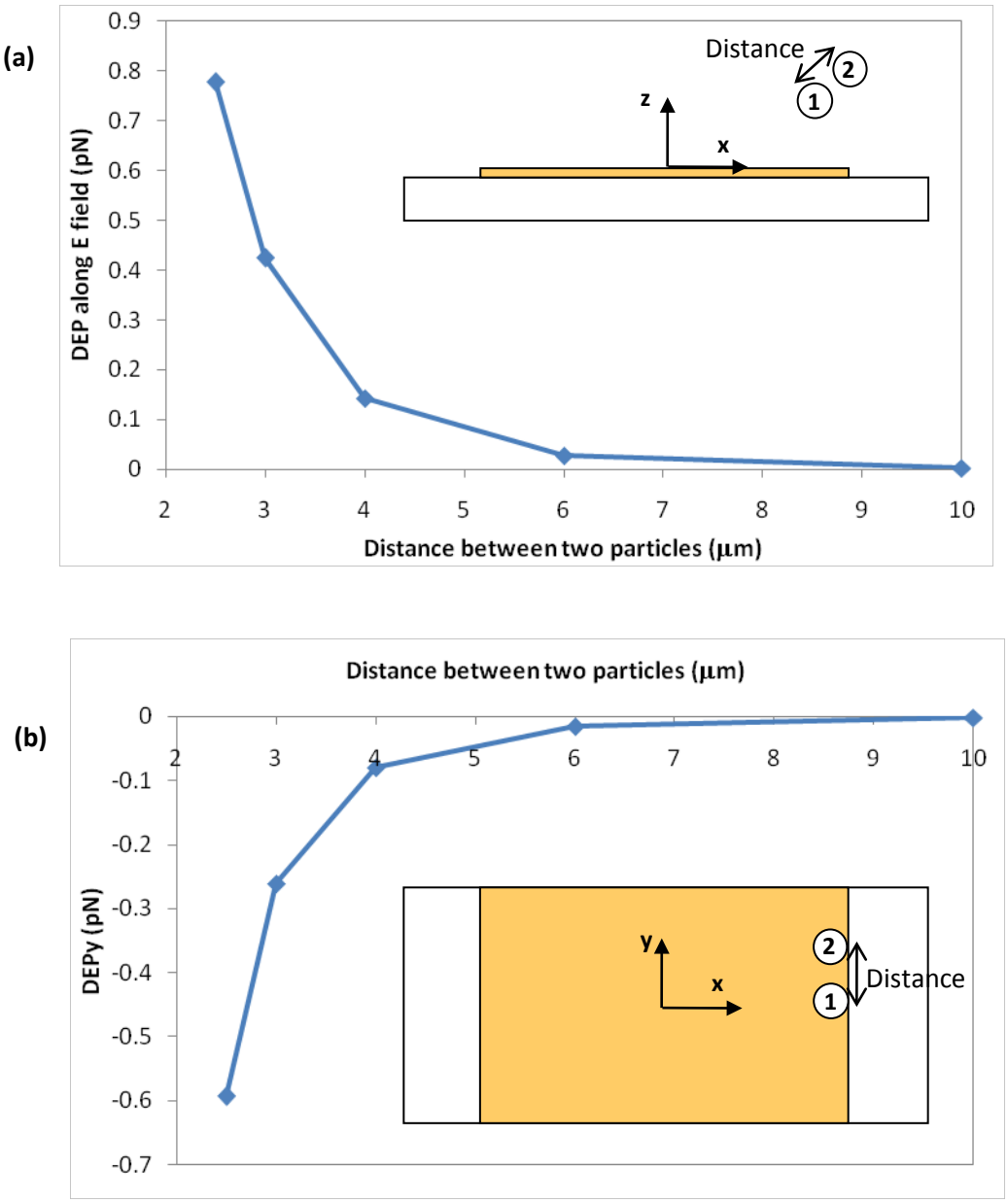

Figure 12 Computed DEP force acting on a bead particle under an ETF condition (σ_m = 1.7 S/m, f = 200 kHz and V_{rms} = 7 V). The subject particle (particle 1) is located at the swirling center (x = 36 μm, y = 0 and z = 27 μm), the neighboring particle approaches in (a) the parallel and (b) the perpendicular directions to the electric field.

3.5 CONCLUSIONS

Polystyrene microbead particles have been investigated and subjected to AC electrothermal flow conditions through experimental and numerical studies. Typical particle behaviors were monitored as the main parameters, such as media conductivity and the frequency of the applied voltage, were varied, and the experimental observations were compared with numerical simulation results. Since the conventional dipole method for DEP calculation does not consider the effect of neighboring particles and other solid surfaces, the Maxwell stress tensor method was applied in our numerical study to understand the dielectrophoretic particle-particle interactions. Distinct particle behaviors under ETE conditions and diverse particle-particle interactions, such as particles keeping a certain distance from each other, chain formation, and disc formation, have been analyzed and explained based on the numerical simulation results. ETE conditions induced particle chain and disc formation 15 μm above the electrode edge, and they remained in rotational motion. The calculation of the attractive and repulsive DEP particle-particle interaction was performed for this case, and the unique particle behaviors were explained. The improved understanding of particle behaviors in AC electrohydrodynamic flows presented here will enable researchers to design better particle manipulation strategies for lab-on-a-chip applications.

Chapter 4: Heterogeneous Immunoassay with AC Electrothermal Mixing

4.1 Microfluidic devices fabrication

4.1.1 SU-8 template fabrication

3 inch Si wafers (University Wafer Inc.) were cleaned with piranha solution (98% sulfuric acid: Hydrogen peroxides = 3:1) for 10 min, followed by 2% HF cleaning for 3 min. After rinsing with DI water, Si wafers were dehydrated at 150°C for 5 min. HMDS (MicroChem Corp.) was coated on Si wafers for better adhesion of SU-8. The wafers were dehydrated for another 5 min at 150°C. Patterned SU-8 photoresist features were formed on Si substrates as follows. Negative photoresist, SU-8 2035 (MicroChem Corp.), was spun on a glass at 1000 rpm for 30 s, which yielded a thickness of 120 μm, followed by soft baking at 65°C and 95°C for 10 min and 30 min respectively. After exposing the photoresist to UV light (19.8 mW/cm^2) through a patterning mask for 30s, the wafer was baked at 65°C and 95°C for 15 min each. Then the SU-8 pattern was developed in SU-8 developer (MicroChem Corp.) for 20 min, and rinsed with isopropanol.

4.1.2. Mixing elements fabrication

The electrothemal flow mixing elements were fabricated on a 4 inch silicon substrate with a 200 nm silicon dioxide isolation layer (University Wafer Inc.). First, 20 nm thick chrome and 200 nm thick gold layers were deposited on the substrate using thermal evaporation. Then a photoresist pattern (Shipley 1827) was made on the metal surface by photolithography (3000 rpm coating and 120mJ/cm^2 dose), and it was used as a masking material during the subsequent etching process. Gold and chrome etching was done with Gold etchant trifluoroacetic acid (TFA) and Chromium mask etchant, respectively

(Transene company). The device with microelectroedes is shown in Figure 13. The fingers of the electrodes are 2 mm long 40 μm wide and are separated by 60 μm gaps.

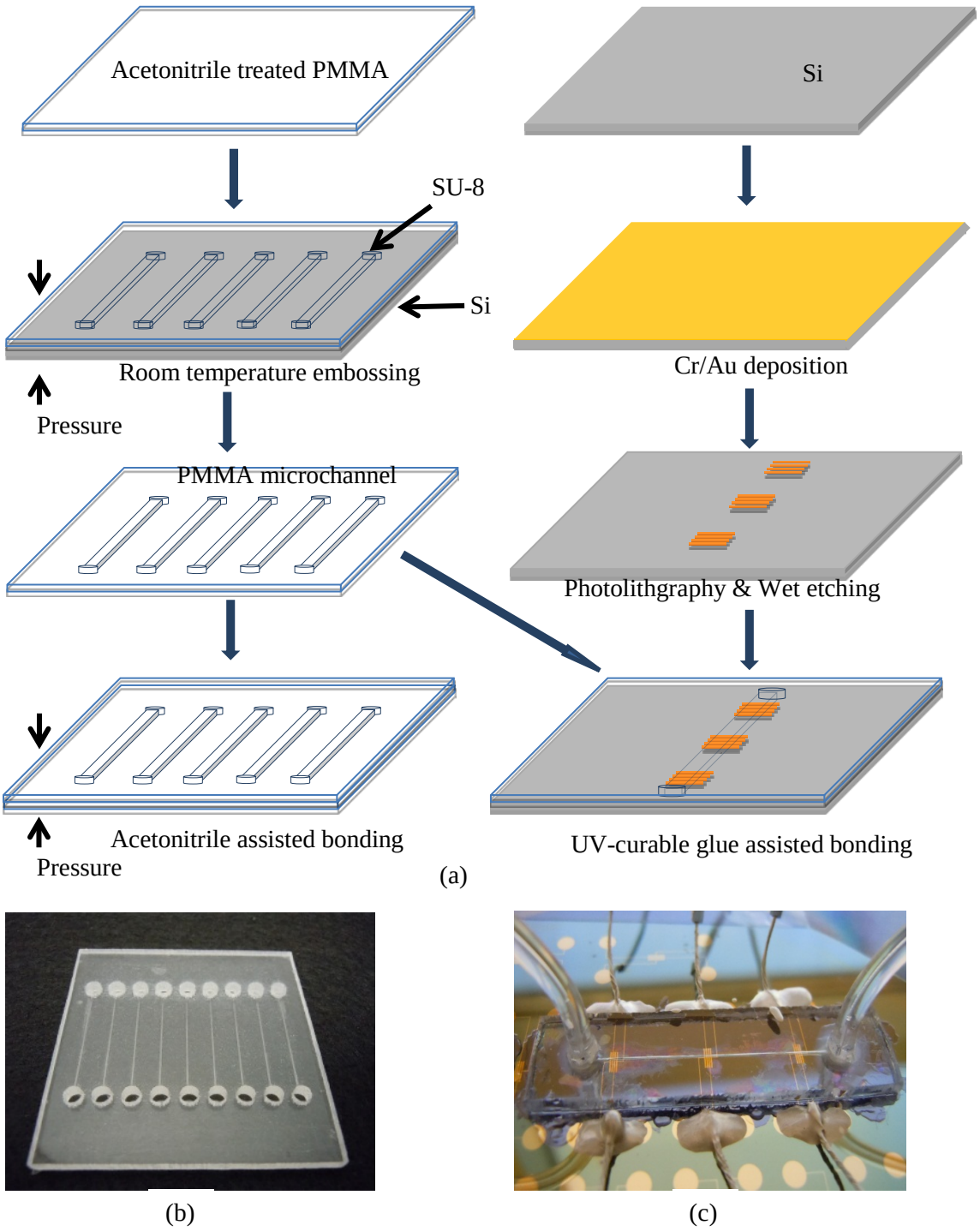

Figure 13 (a) Schematic of fabrication process. (b) All PMMA microfluidic device. (c) Si/PMMA microfluidic device.

4.1.3. Channel imprinting and PMMA bonding

Acetonitrile assisted PMMA-PMMA bonding was adopted and modified based on the method of Sun et al [37]. Briefly, laser-cut 2 inch by 2 inch PMMA pieces (McMaster) were ultrasonicated in isopropanol for 5 min, rinsed with DI water and dried under nitrogen. 500 μl of acetonitrile was dispensed on the surface of PMMA substrates, which were then covered with a clean glass slide and transferred to a sealed container. After 10 min, the SU-8 patterned Si substrate was pressed into one solvent-wetted surface with a pressure of 1000 lb for 30 min. The imprinted PMMA piece and another acetonitrile softened piece were bonded together by manually applying gentle pressure.

In order to achieve PMMA-SiO_2 bonding, a UV curable glue, NOA 84 (Norland Product Inc., NJ, USA) was used to assist bonding. Single channel pieces were cut from the imprinted pieces above. Then the microchannel was vertically aligned with fabricated electrodes, and a clamp was used to hold the assembly together. A UV-curable adhesive resin was introduced between the contact area of PMMA channels and silicon substrate. The resin filled up the gap due to capillary action but the microchannel was kept open (the resin did not continue flowing into the microchannel) due to the capillary pressure drop. 3 min UV exposure was applied to complete the bonding process.

4.2 PMMA functionalization and MPO assay

4.2.1 PMMA functionalization

PMMA material was first treated with NaOH to hydrolyze the ester group on the surface of PMMA, releasing carboxyl group for further functionalization, a method developed by Bai et al. [38]. The method was modified slightly. 1N NaOH at 60°C was pumped through the channels using a peristaltic pump (100µl/min) for 1 hour, followed by washing with 0.1M PBS buffer (pH 7.4). The hydrolyzed PMMA channels were then treated with 0.2% PEG (2000 g/mol) for 1 hour at room temperature followed by circulating 1% glutaraldehyde for 30 minutes. The PMMA surface was thoroughly rinsed with DI water after each treatment step.

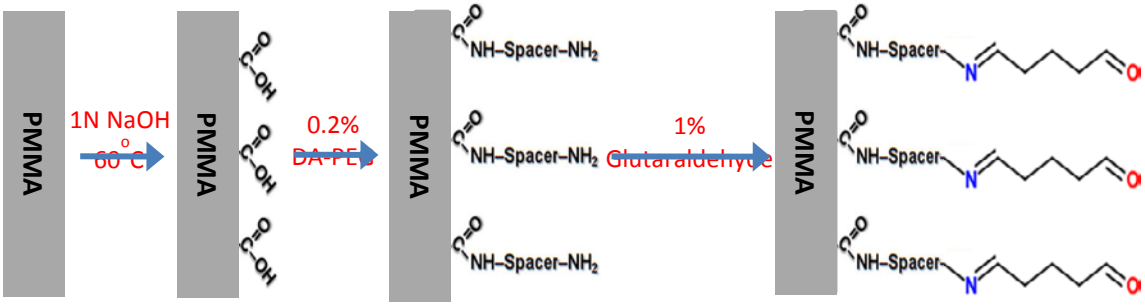

Figure 14: Schematic of PMMA surface functionalization.

4.2.2 Sandwich type MPO assay

In the all-PMMA microchannel device, incubation of 200 nM (~30μg/ml) of rabbit anti-human polyclonal MPO antibody (ABD Serotec, NC, USA) for 1 hour was followed by blocking with 2% BSA for 30 minutes. 0-41.7nM (~0-6.25μg/ml) MPO (Lee Biosolutions, St. Louis, MI, USA), 66.7nM (~10μg/ml) biotin labeled mouse anti-human monoclonal MPO antibody (US Biological Inc.), and 20nM streptavidin labeled QDs (λ_{em} = 605nm, from Invitrogen) were incubated for 1 hour at room temperature. The microchannels were thoroughly washed with 100μl of 0.1M PBS containing 0.01% Tween-20.

Immunoassay with ETE was based on the similar procedure as mentioned above. An electric field was applied during MPO, biotin-mAb, and streptavidin-QD incubation steps for 5 min, instead of incubating at room temperature for 1 hour without ETE. Everything else was the same as the standard protocol above.

4.3 Results and discussion

4.3.1 Velocity: numerical model and experiment observation

The particle movement due to ETE was observed as the amplitude and the frequency of the applied voltage was varied. At a high frequency (200kHz) condition, ACEO does not exist, while ETE is dominant in this condition. Below $3V_{rms}$ no particle motion was observed. As the voltage was increased, particles became more and more active until the electrodes were damaged at $10V_{rms}$. The experimental results had a good agreement with the numerical simulation shown in Figure 15. For immunoassay, a large scale and mild fluidic hydrodynamic motion is desired. Thus, a set of parameters ($6V_{rms}$, 200kHz) was chosen for immunoassay experiments.

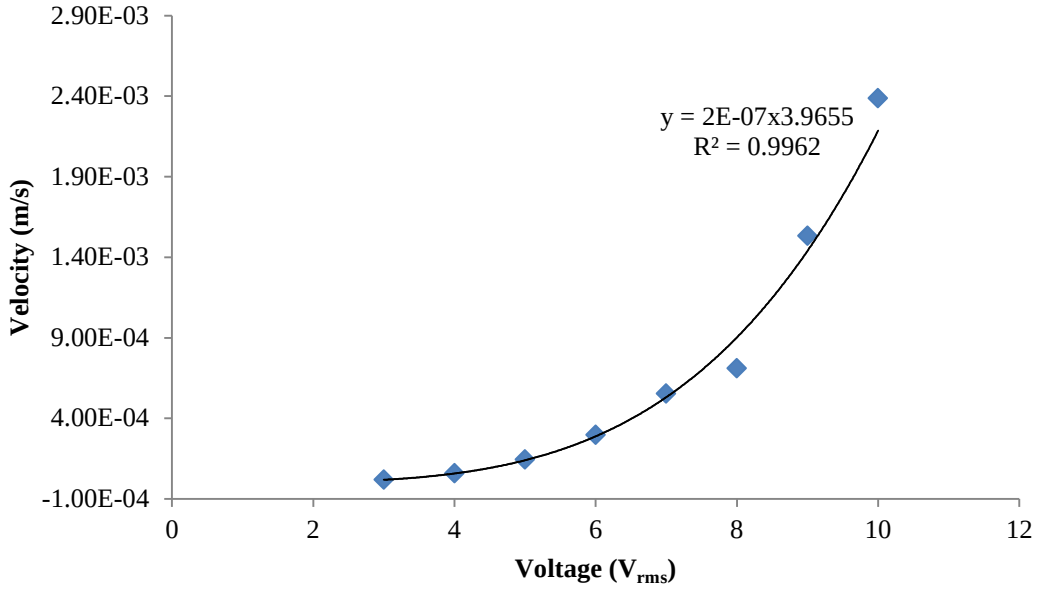

Figure 15 Numerical simulation result of fluid velocity as a function of the applied voltage. Frequency was fixed at 200kHz. At 6 Vrms, the velocity is 296 μm/s.

4.3.2 Oprimization of optical detection system

As shown in Figure 16, the optical setup is comprised of a firewire monochrome CCD camera (Stingray, AVT-FS-033B), a UV-LED rated at 27 mW optical power, an excitation filter was used to cut off other light source, only keeping the desirable excitation light, and another bandpass filter (600±20) was mounted on the detection side to remove any interfering signal. An aspheric lens served the purpose of concentrating the UV light to a spot size of ~1.5 mm. The angle between the UV source and CCD camera was maintained at 60º. A serial dilution of QD 605 streptavidin was prepared to test the sensitivity of the optical detection system, and it was repeated three times. In order to generate high power of the UV source while protecting the LED from burning down, the power supply constantly offered 5 V, 0.5 Amp power to the UV-LED.

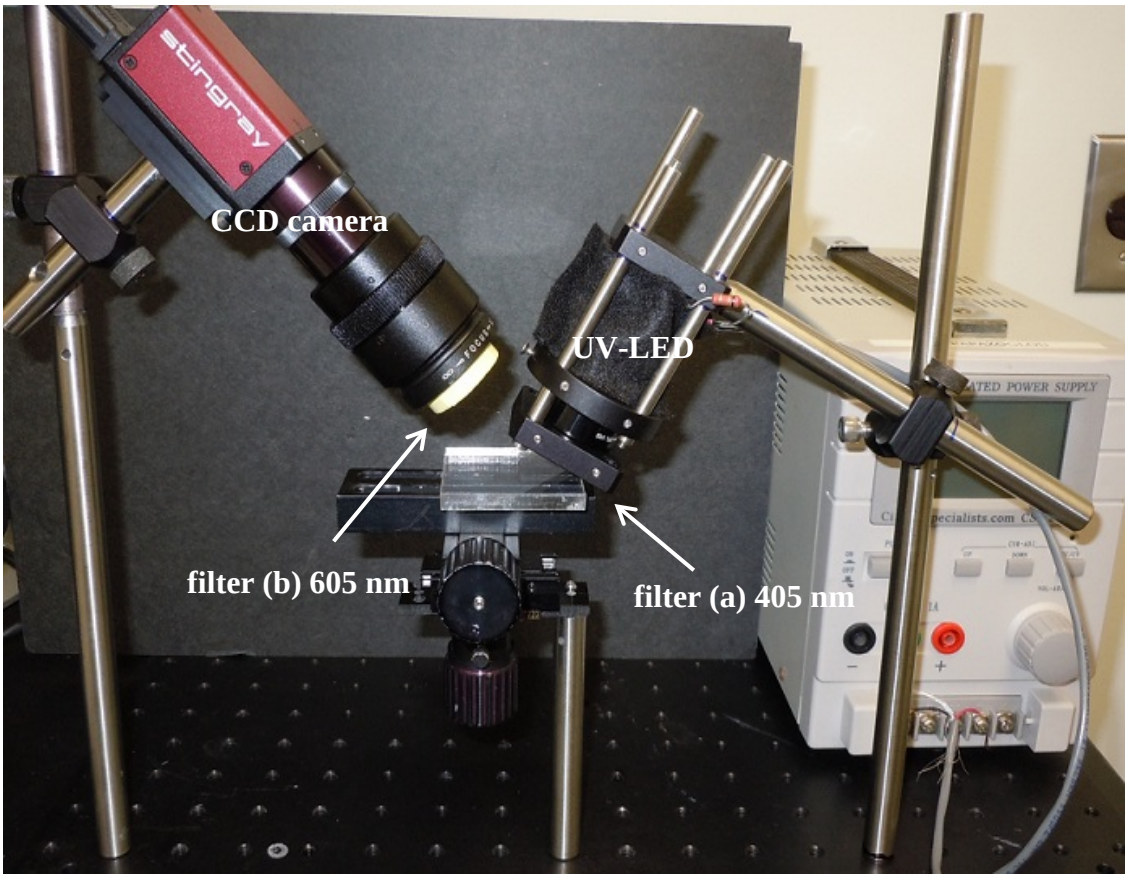

Figure 16 Optical setup for fluorescence signal collection from quantum dots.

4.3.2.1 Cameras settings optimization

Different camera parameters such as shutter speeds and gains were tested to improve the performance of the optical setup, by obtaining a large dynamic range of fluorescent signal at low concentration of quantum dot (0 ~ 1 nM). It was found, as shown in Figure 17, a large dynamic range of signal can be achieve by tuning the camera settings when shutter speed equals to 200 us (890 ms) and gain equals to 340.

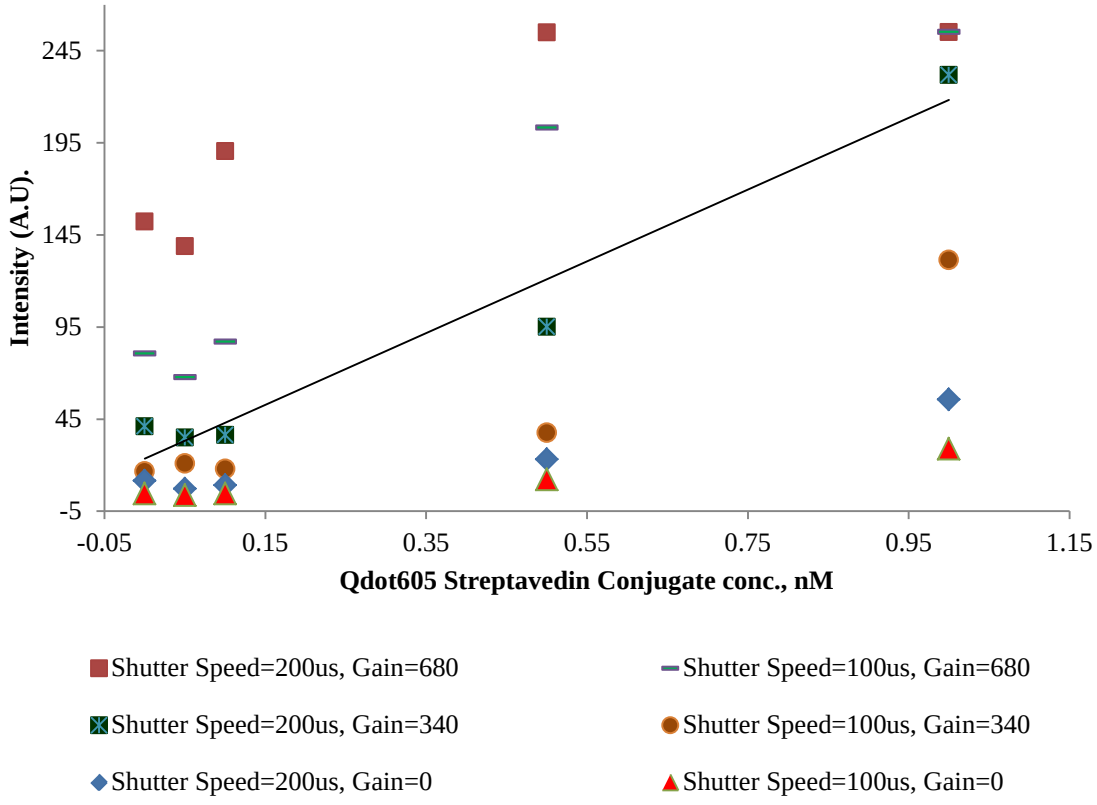

Figure 17 Camera Settings test.

4.3.2.2 Cameras comparision

In order to improve the sensitivity of the detection system, a new firewire monochrome CCD camera (F-125B) was purchased from Stingray. The F-125B has higher resolution, 1292 x 964 pixels, compared to 656 x 492 pixels on F-033B. The most important feature is the F-125B has quantum efficiency above 50% at 600 nm wavelength, which is the QD 605 emission wavelength, whereas, F-003B has a quantum efficiency below 35% at 600 nm. However, the testing result, figure 18, shows that the old camera actually perform better than the new one. The sensitivity was not improved above previously established limit of about 0.5 nM of QDs in 1 x PBS buffer. At the same concentration of QDs, F-033B camera gave about 40 – 50% higher signal than F-125B, using the same shutter time and gain settings. After further investigating the specifications of both cameras on data sheets, it is found that F-033B has a 1/2“ CCD sensor, which is larger than that of F-125B (1/3“). This indicates that with a larger sensing part, F-033B can receive more photons than F-125B. Higher resolution should be an advantage of F-125B, however, since the sensor size is only 1/3“, the pixel size on it is 3.75 x 3.75 μm. Compared to the 9.9 x 9.9 μm pixel size on F-033B, the new camera is not as good as the old one. Thus, the detection system switches back to the old camera.

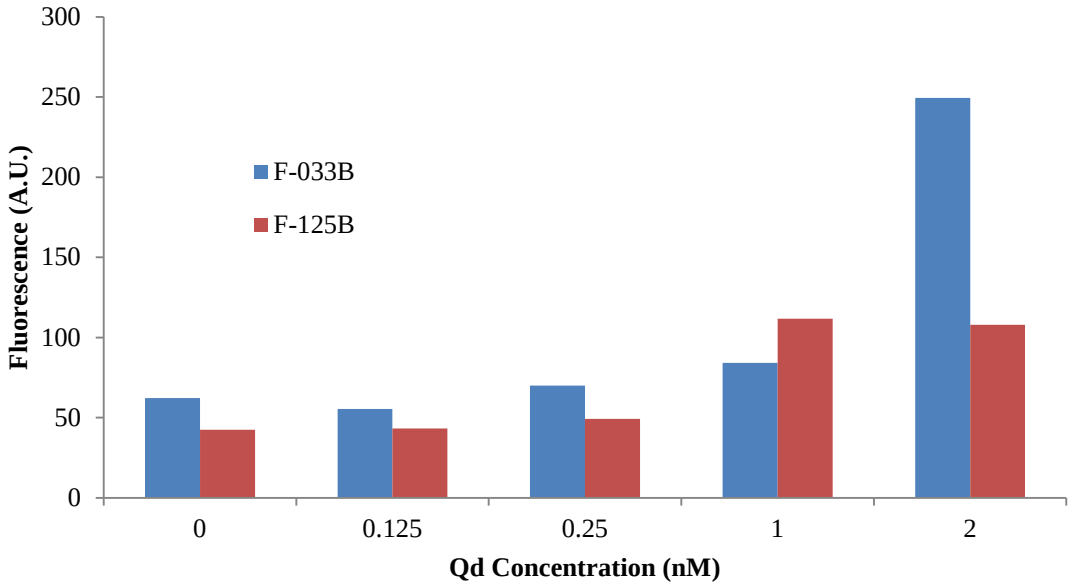

Figure 18 Old camera shows better performance over new camera.

4.3.3 MPO assay in PMMA/PMMA devices

Immunoassay was carried out based on a typical pAb/MPO/QD-mAb sandwich assay. In all the immunoassay, 10nM of QD 605 streptavidin was used. The concentration was more than enough (5 nM) to saturate the camera. QD streptavidin conjugate could be conjugated with biotin-mAb complex beforehand. However, this additional step may cause a loss in the amount of antibody as well as QD during the separation of QD-mAb complex from QD and antibody.

BMP image data collected from the CCD were analyzed and resulted in quantification of the concentration of MPO based on the fluorescence intensity of the QD. A region of interest (ROI), typically 15×40, was chosen at the geometrical center of the microchannel. An average of the intensities of all the pixels within the ROI was obtained using ImageJ.

Though the dominant binding mode is one QD streptavidin conjugate per analyte, it should be noted that there are typically 5-10 streptavidins covalently attached on the surface of each quantum dot according to the protocol provided Invitrogen. When the concentration of the analyte, MPO in this case, is low, QD streptavidin conjugate react with biotin-mAb by 1:1 ratio. However, when the concentration of MPO exceeds the saturating concentration, it is expected that one QD may bind to more than one pAb-MPO-mAb complex, resulting in artificially reduced signals. This assumption fits with the experimental result. In the Figure 19, there is a clear signal intensity drop , which indicates that given the concentration of QD, the pAb-MPO-mAb complex was reach the saturation concentration at 20nM.

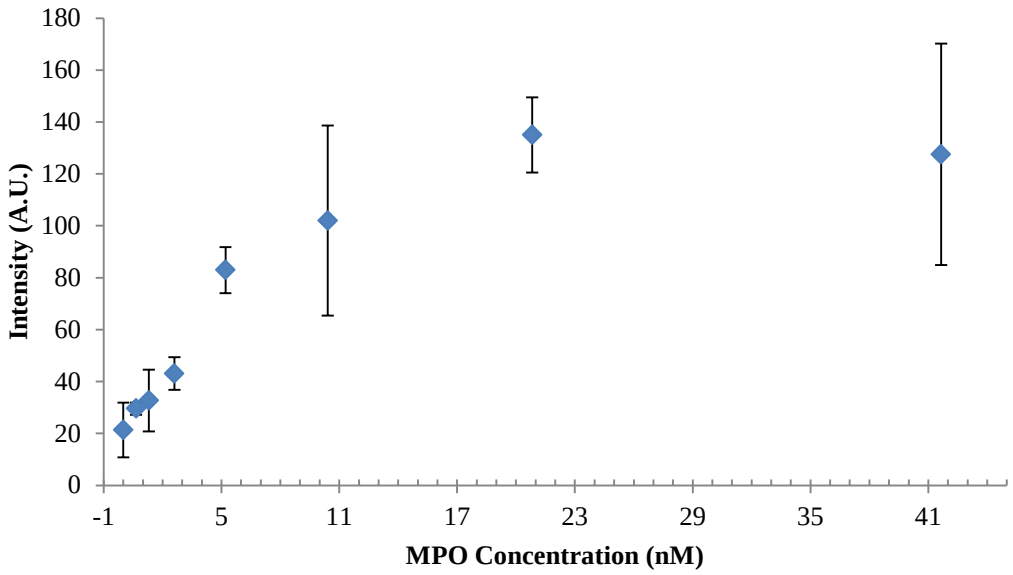

Figure 19 Calibration curve for the sandwich QLIDA in all PMMA microfluidic device. The data points are the average of three independent measurements performed with three different microchannel devices.

4.3.4 MPO assay in Si/PMMA devices

The imaged results are shown in Figure 20. Figure 20(b) shows a typical control case assay that was allowed to react for 5 minutes with no electrothermal mixing. Figure 20(c) is a typical assay that was performed and enhanced with the electrothermal mixing for the same time period, 5 minutes. The electrodes were energized with an applied potential of $6V_{rms}$ and a frequency of f = 200 kHz for 5 min. The brighter fluorescent spot indicates improved binding and a faster reaction. The images were taken from near the mixing electrodes area rather directly from the electrodes area, due to the fact that reflection from the gold electrodes interfered the detection by increasing the background signal.

Quantification of the image data was achieved through fluorescent intensity measurements using ImageJ. The results are shown in Figure 20. Without ETE mixing, the fluorescent signal was very low, indicating that there is limited binding between pAb and MPO, and between MPO and QD-mAb within 5 minutes. However, with ETE mixing, the binding efficiency was greatly improved, and signal intensity was comparable to the normal MPO assay with 1 hour incubations.

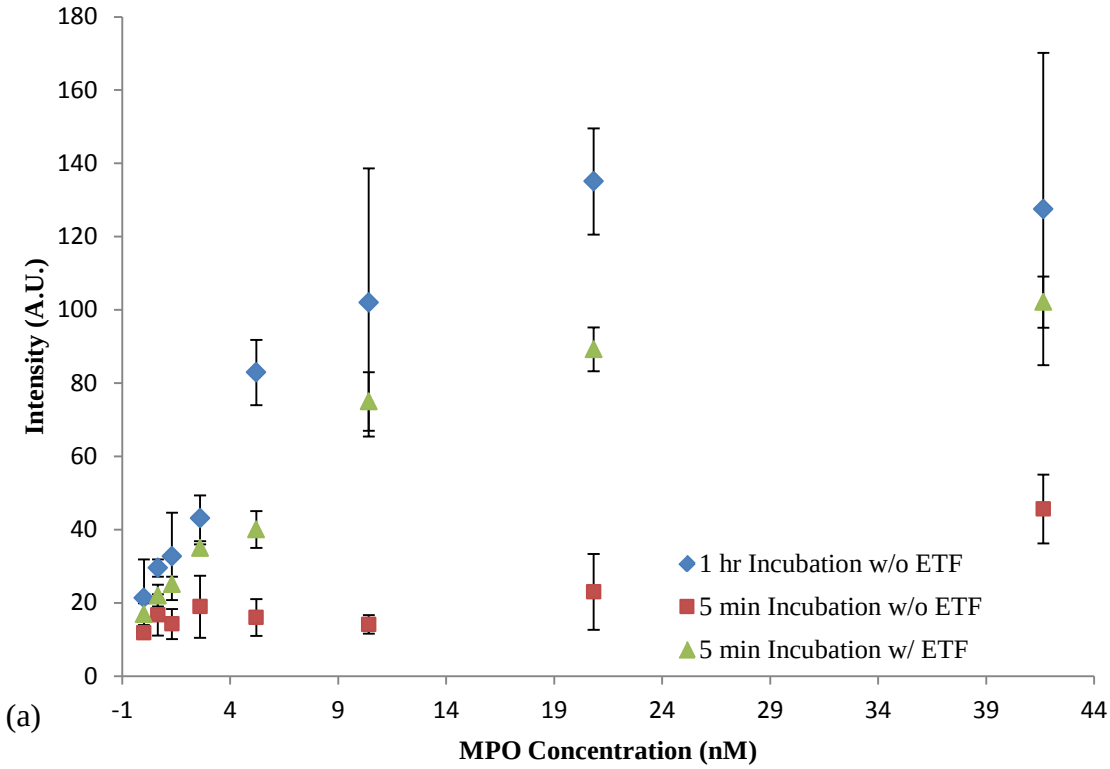

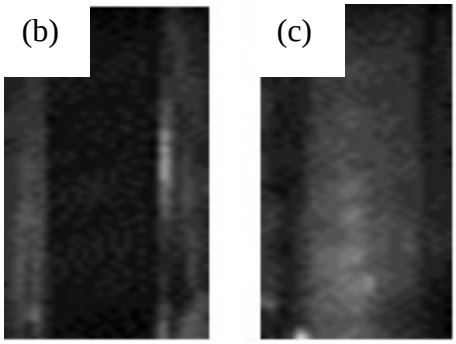

Figure 20 QLIDA assay intensity with and without electrpthermal flow (ETE) mixing 5minutes. (a) Significant increase in the intensity is observed with ETE mixing. (b) result with ETE mixing (left), and result without ETE mixing (right).

4.4 Conclusions

Two types of microfabricated QLIDA biosensor were successfully designed, and MPO immunoassay was successfully conducted with the QLIDA biosensor. Different camera parameter settings have been tested and optimized specifically for 605 nm emission spectrum quantum dots. Straptavidin labeled quantum dots were finally chosen for this biosensor system as a detecting probe, due to the fast reaction and strong binding of biotin to straptavidin. Fluidic motion under the electrothermal effect condition was observed and investigated for the microfabricated QLIDA biosensor with embedded ETE mixing. The optimal voltage was chosen for eletrothermal effect mixing in microfluidic biosensors. An optical detection system was built for QLIDA microfluidic biosensors. With the enhancement of the electrothermal effect, the reaction and response time could be significantly shortened. With an active mixing element, the detection time was significantly reduced from about 3.5 hours to 30 minutes.

Chapter 5: Summary

5.1 Conclusion

Microfabricated Quantum dot Linked Immuno-Diagnostic Assay (QLIDA) biosensor was successfully designed, and MPO immunoassay was successfully conducted with the QLIDA biosensor. Quantum dot was chosen for this biosensor, for its unique optical properties that better than conventional fluorescent dyes or fluorescent probes. Optical detection system was carefully investigated and tested for this specific biosensor. In order to achieve fast detection, AC electrothermal effect, one of three AC electrokinetic phenomena, was chosen and integrated into the microfabricated biosensor platform. Fluidic motion under the electrothermal flow was characterized, and optimal operation parameters for ETE in the biosensor were set at 6 V_{rms}, 200 kHz. Antibody and antigen binding efficiency is enhanced by disturbing the "tranquility" of diffusion based delivery. ETE increases the vertical fluid velocity, actively transporting antibody and antigen to the sensing part of QLIDA biosensor, which is the ceiling of the biosensor, in this case. By doing this, antibody and antigen have a higher chance to binding to the receptors on the sensing part. With the enhancement of the electrothermal effect, the reaction and response time could be significantly shortened. With an active mixing element, the detection time was significantly reduced from about 3.5 hours to 30 minutes.

Particle behaviors also have been investigated under AC electrothermal flow conditions through experimental and numerical studies. 2 μm polystyrene microbeads were used in this study. Typical particle behaviors were monitored as the main parameters, such as media conductivity, frequency, and applied voltage, were varied. Distinct particle

behaviors under ETE conditions and diverse particle-particle interaction, such as “pearl chain” formation, “disc” formation, have been analyzed and explained based on the numerical simulation results. Unique particle behaviors were due to the interaction between hydrodynamic force caused by ETE and attraction/repulsion force caused by DEP.

5.2 Future work

In this study, microfabricated Quantum dot Linked Immuno-Diagnostic Assay biosensor was successfully developed, thereby laying foundation for future development.

In order to improve the sensitivity of the immunobiosensor, different surface functionalization methods for antibody immobilization could be employed. Chemical, such as acid, or physical methods, such as UV light, can be used to release carboxyl group of PMMA in the first step, which if well achieved could be a good foundation for the following steps. Also, there are various way to immobilize antibody on the PMMA that are worthy investigation. Operation parameter for ETE can be further studied in terms of voltage, frequency, applying time, and so on.

The design of microfluidic chip can be further studied. A heating element can be added into the channel along with the mixing element, so as to improve antibody and antigen binding efficiency. More components, such as reagent chamber, waste reservoir, can be included into the microfluidic chip to achieve semi/full-automation. Sample dilution, or standard curve, can also be obtained on the microfluidic chip if incorporate the microfluidic chip with delay circuits – essentially controlling the amout and rate at which two fluids mix.

Meanwhile, not only other cardiac biomarkers, such as Troponin I, Troponin T, but also other biomarkers can be tested on QLIDA biosensor for feasibility.

All the above ideas can be implemented in future to improve the performance of the current Quantum dot Linked Immuno-Diagnostic Assay biosensor, and board the applications of the QLIDA biosensor.

List of References

1. Crowther, J.R., *The ELISA guidebook.* Methods Mol Biol, 2000. **149**: p. III-IV, 1-413.

2. Schneider, U.V., et al., *The prognostic value of the suPARnostic ELISA in HIV-1 infected individuals is not affected by uPAR promoter polymorphisms.* BMC Infect Dis, 2007. **7**: p. 134.

3. Tehe, A., et al., *Quantification of HIV-1 p24 by a highly improved ELISA: an alternative to HIV-1 RNA based treatment monitoring in patients from Abidjan, Cote d'Ivoire.* J Clin Virol, 2006. **37**(3): p. 199-205.

4. Munene, E., et al., *Evaluation of HIV ELISA diagnostic kit developed at the Institute of Primate Research, Nairobi, Kenya.* Afr J Health Sci, 2002. **9**(3-4): p. 117-22.

5. Abbott, M., et al., *Validation procedures for quantitative food allergen ELISA methods: community guidance and best practices.* J AOAC Int, 2010. **93**(2): p. 442-50.

6. Patrick, W., S. Hans, and P. Angelika, *Determination of the bovine food allergen casein in white wines by quantitative indirect ELISA, SDS-PAGE, Western blot and immunostaining.* J Agric Food Chem, 2009. **57**(18): p. 8399-405.

7. Granito, A., et al., *Antifilamentous actin antibodies by ELISA for the diagnosis of type 1 autoimmune hepatitis.* Am J Gastroenterol, 2007. **102**(5): p. 1131-2.

8. Aubert, V., I.G. Pisler, and F. Spertini, *Improved diagnoses of autoimmune hepatitis using an anti-actin ELISA.* J Clin Lab Anal, 2008. **22**(5): p. 340-5.

9. Ottino, J.M. and S. Wiggins, *Introduction: mixing in microfluidics.* Philos Transact A Math Phys Eng Sci, 2004. **362**(1818): p. 923-35.

10. Babu, S., et al., *A PMMA microcapillary quantum dot linked immunosorbent assay (QLISA).* Biosens Bioelectron, 2009. **24**(12): p. 3467-74.

11. Rasooly, A., *Biosensor technologies.* Methods, 2005. **37**(1): p. 1-3.

12. Wilson, G.S. and Y. Hu, *Enzyme-based biosensors for in vivo measurements.* Chem Rev, 2000. **100**(7): p. 2693-704.

13. Llandro, J., et al., *Magnetic biosensor technologies for medical applications: a review.* Med Biol Eng Comput, 2010. **48**(10): p. 977-98.

14. Hines, J.W., *Medical and surgical applications of space biosensor technology.* Acta Astronaut, 1996. **38**(4-8): p. 261-7.

15. Mataveli, L.R., et al., *Evaluation of a simple and low cost potentiometric biosensor for pharmaceutical and in vivo adrenaline determination.* Biosens Bioelectron, 2010. **26**(2): p. 798-802.

16. Sezginturk, M.K., A.S. Akin, and E. Dinckaya, *A biosensor utilizing quince (Cydonia vulgaris) tissue homogenate for dopamine determination in pharmaceutical preparations.* Prep Biochem Biotechnol, 2010. **40**(2): p. 129-38.

17. Wang, H., et al., *Development of biosensor-based SPR technology for biological quantification and quality control of pharmaceutical proteins.* J Pharm Biomed Anal, 2009. **50**(5): p. 1026-9.

18. Campanella, L., et al., *New biosensor for superoxide radical used to evidence molecules of biomedical and pharmaceutical interest having radical scavenging properties.* J Pharm Biomed Anal, 2000. **23**(1): p. 69-76.

19. Karyakin, A.A., et al., *Optimal environment for glucose oxidase in perfluorosulfonated ionomer membranes: improvement of first-generation biosensors.* Anal Chem, 2002. **74**(7): p. 1597-603.

20. Tamayo, J., et al., *Chemical sensors and biosensors in liquid environment based on microcantilevers with amplified quality factor.* Ultramicroscopy, 2001. **86**(1-2): p. 167-73.

21. Baeumner, A.J., *Biosensors for environmental pollutants and food contaminants.* Anal Bioanal Chem, 2003. **377**(3): p. 434-45.

22. Rasooly, A. and K.E. Herold, *Biosensors for the analysis of food- and waterborne pathogens and their toxins.* J AOAC Int, 2006. **89**(3): p. 873-83.

23. Patel, P.D., *Overview of affinity biosensors in food analysis.* J AOAC Int, 2006. **89**(3): p. 805-18.

24. Indyk, H., *Biosensors: making sense of food.* J AOAC Int, 2006. **89**(3): p. 804.

25. Piryatinski, A., et al., *Effect of quantum and dielectric confinement on the exciton-exciton interaction energy in type II core/shell semiconductor nanocrystals.* Nano Lett, 2007. **7**(1): p. 108-15.

26. Morgan, H., *Editorial: AC electrokinetics of molecules and macromolecular assemblies.* IEE Proc Nanobiotechnol, 2003. **150**(2): p. 37-8.

27. Pohl, H.A. and J.S. Crane, *Dielectrophoresis of cells.* Biophys J, 1971. **11**(9): p. 711-27.

28. Ahualli, S., et al., *AC electrokinetics of concentrated suspensions of soft particles.* Langmuir, 2009. **25**(4): p. 1986-97.

29. Thomas, R.S., H. Morgan, and N.G. Green, *Negative DEP traps for single cell immobilisation.* Lab Chip, 2009. **9**(11): p. 1534-40.

30. Peitz, I. and R. van Leeuwen, *Single-cell bacteria growth monitoring by automated DEP-facilitated image analysis.* Lab Chip, 2010. **10**(21): p. 2944-51.

31. Ahmed, M.U., et al., *Electrochemical DNA biosensor using a disposable electrochemical printed (DEP) chip for the detection of SNPs from unpurified PCR amplicons.* Analyst, 2007. **132**(5): p. 431-8.

32. Oh, J., et al., *Comprehensive analysis of particle motion under non-uniform AC electric fields in a microchannel.* Lab Chip, 2009. **9**(1): p. 62-78.

33. Lide, D.R., *CRC Handbook of Chemistry and Physics*. 2000, New York: CRC Press.

34. Green, N.G., Morgan, H., *AC Electrokinetics: colloids and nanoparticles*. 2002, England: SRP Ltd.

35. Oh, J., et al., *Comprehensive analysis of particle motion under non-uniform AC electric fields in a microchannel.* Lab on a Chip, 2009. **9**(1): p. 62-78.

36. Green, N.G., et al., *Fluid flow induced by nonuniform ac electric fields in electrolytes on microelectrodes. I. Experimental measurements.* Phys Rev E Stat Phys Plasmas Fluids Relat Interdiscip Topics, 2000. **61**(4 Pt B): p. 4011-8.

37. Sun, X., et al., *Rapid prototyping of poly(methyl methacrylate) microfluidic systems using solvent imprinting and bonding.* Journal of Chromatography A, 2007. **1162**(2): p. 162-166.

38. Bai, Y., et al., *Surface Modification for Enhancing Antibody Binding on Polymer-Based Microfluidic Device for Enzyme-Linked Immunosorbent Assay.* Langmuir, 2006. **22**(22): p. 9458-9467.